

Supporting Information for

Recessed Gold Nanoring-Ring Microarray Electrodes

Mahdieh Atighilorestani^{1,2} and Alexandre G. Brolo^{1,2*}

¹Department of Chemistry, University of Victoria, P.O. Box 1700, STN
CSC, Victoria BC V8W 2Y2, Canada

²Center for Advanced Materials and Related Technologies (CAMTEC), University
of Victoria, Victoria, BC, V8W 2Y2, Canada

*E-mail: agbrolo@uvic.ca. Phone: (+1)-250-721-7167. Fax: (+1)-250-721-7147.

TABLE OF CONTENTS

Page S-4– Figure S-1. Schematic representation of the Au-NRRA fabrication process.

Page S-7– Figure S-2. Optimization of the FIB fabrication parameters using Z-contrast imaging.

Page S-9– Simulation details.

Page S-12– Figure S-3 Concentration profiles for the 6×6 Au-NRRA operating with and without redox cycling.

Page S-13– Figure S-4. Schematic representations of the 6×6 Au-NRRA operating with and without redox cycling.

Page S-14– Figure S-5. Schematic representation of the unit cell for a 6 × 6 recessed generator-collector nanoring-ring microarray

Page S-15– Figure S-6. Influence of varying ring height on the simulated cyclic voltammograms for the 6×6 Au-NRRAs represented base on the limiting current and current density

Page S-16– Table S-1a. Influence of the varying ring height on the 6×6 Au-NRRA performance.

Page S-17– Table S-1b. Influence of the varying ring height on the 6×6 Au-NRRA performance.

Page S-18– Table S-1c. Influence of the varying ring height on the 6×6 Au-NRRA performance.

Page S-19– Figure S-7. Influence of varying hole radius on the simulated cyclic voltammograms for the 6×6 Au-NRRAs represented base on the limiting current and current density

Page S-21 – Figure S-8. Surface concentration profiles for species O within the hole next to the electrode surface for the Au-NRRA with different heights (25 nm, 50 nm, 75 nm, 100 nm).

Page S-23 – Figure S-9. Volume concentration profiles (revolution 2D) for species O within the hole next to the electrode surface for the Au-NRRA with different heights (25 nm, 50 nm, 75 nm, 100 nm).

Page S-25– Figure S-10. Simulated cyclic voltammograms under various scan rates for the 6×6 Au-NRRA.

Page S-26– Table S-2. Influence of the scan rate on the 6×6 Au-NRRA performance.

Page S-28– Figure S-11. Comparison of simulated cyclic voltammograms for the 6×6 Au-NRRAs (operating in redox cycling mode) with different interelectrode gaps.

Page S-29– Figure S-12. Simulated cyclic voltammograms under various scan rates for a 6×6 Au-NRRA with different inter-electrode gap operating in redox cycling mode.

Page S-30– Figure S-13. Dependence of the limiting current on the inter-electrode gap (the gap between generator and collector electrodes).

Page S-31– Table S-3. Influence of the inter-electrode gap on the 6×6 Au-NRRA performance.

Page S-32– Figure S-14. Surface concentration profiles for species O within the hole next to the electrode surface for the Au-NRRA with different inter-electrode gaps (25 nm, 50 nm, 100 nm, 150 nm, 250 nm, 350 nm).

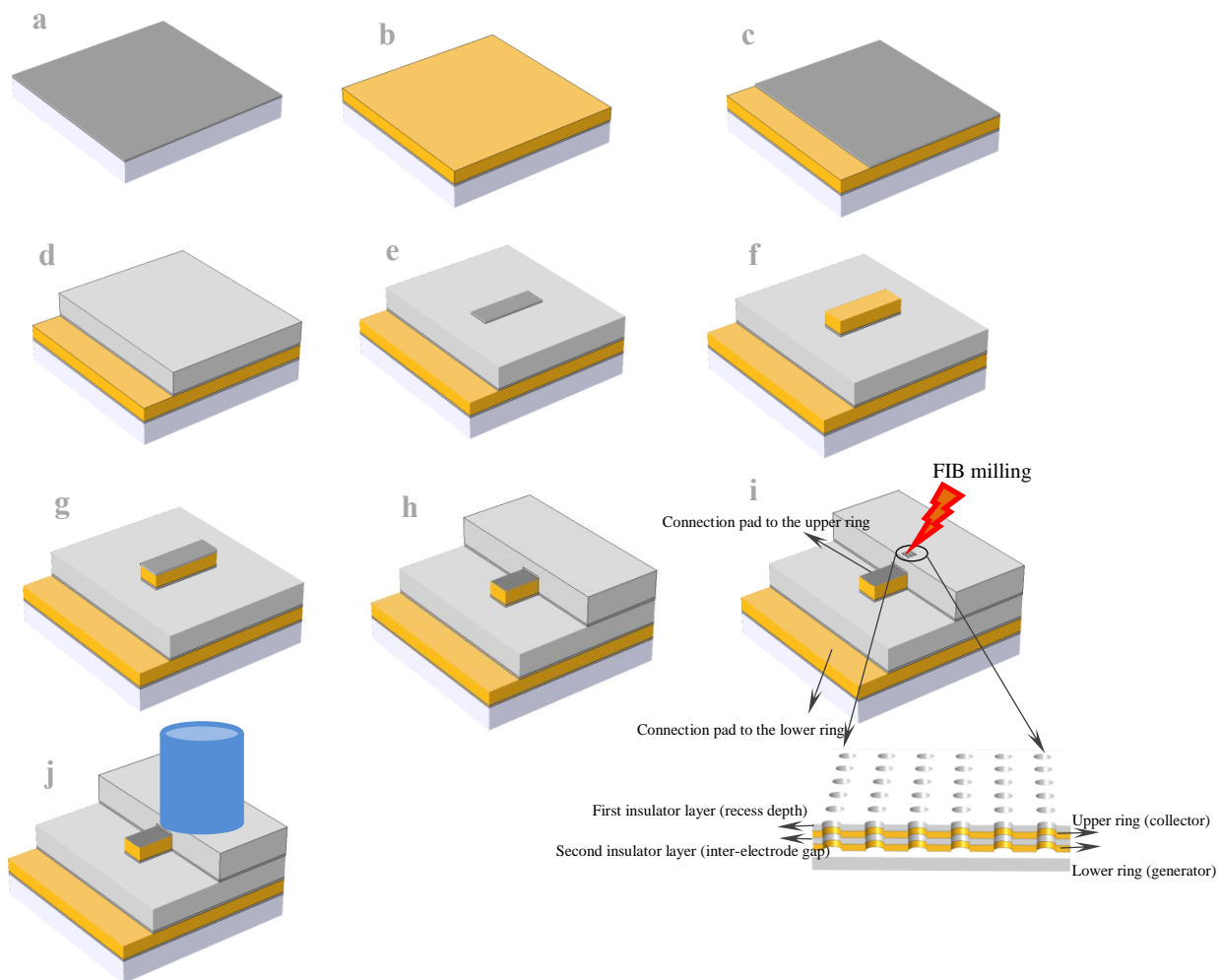
Page S-33– Figure S-15. Volume concentration profiles (revolution 2D) for species O within the hole next to the electrode surface for the Au-NRRA with different inter-electrode gaps (25 nm, 50 nm, 100 nm, 150 nm, 250 nm, 350 nm).

Page S-34– Notes on amplification factor

Page S-36– Table S-4. Demonstration of dependency of the amplification factor on the array size.

Page S-37 – References

Figure S-1. Schematic representations of the Au-NRRA fabrication process (a-j). All the layers in the (Ti (7nm) / Au (50 nm) / Ti (7 nm) / SiO₂ or SiN_x(150 nm) / Ti (7 nm) / Au (50 nm) / Ti (7 nm) /SiO₂ or SiN_x (150 nm)) stack were sputtered using Mantis[®] QUBE sputter deposition system, except for the SiN_x layer which was deposited using plasma-enhanced chemical vapor deposition method. Dimensions are not down to scale. Note that, in contrast to the fabrication process described in ref 1 (which was a combination of standard photolithography, layer-by-layer deposition, and FIB milling), our fabrication process only included the layer-by-layer deposition steps and FIB milling. In the previous study¹, the areas of the electrodes and connection pads were defined using standard photolithography technique. Instead, we have designated these features simply by defining those specified areas using Teflon tape masks during the depositions. In short, our fabrication process was simpler and included fewer fabrication steps in comparison with the previous study¹. It is important to emphasize that standard photolithography involves several steps, including photoresist spin coating, baking the samples to cure the photoresist, illuminate the photoresist through a photomask to pattern the sample and the lift-off step. By eliminating the photolithography, we then significantly simplified the fabrication. Moreover, our process resulted in very clean samples, since we did not have to be concerned with photoresist residues.



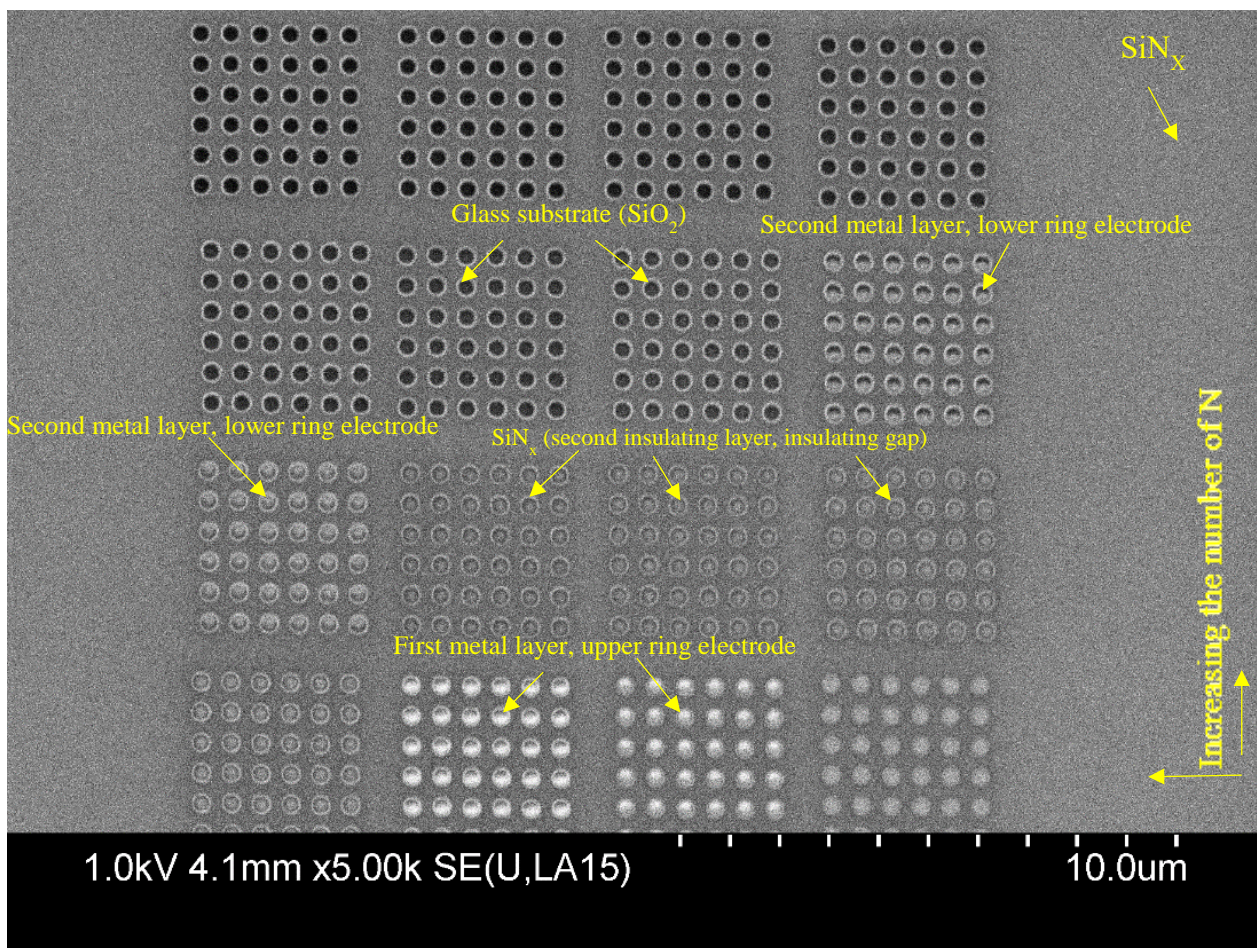
- a) A 7 nm Ti was sputtered over the whole cleaned ($\sim 9 \text{ mm} \times 9 \text{ mm}$) glass slides. The Ti layer was used to improve the adhesion of subsequent gold layer onto the glass substrates.
- b) A 50 nm thick gold film was then sputtered over the Ti adhesion layer on the entire glass slides.
- c) Once the gold was deposited, one edge of the glass substrates was wrapped with Teflon tape to protect the metal film on that area. This protected region was later used as the electrical contact pad on the first gold layer (lower nanoring electrodes). Next, a 7 nm Ti adhesion film was sputtered.

- d) Subsequently, a 150 nm thick SiO₂ (or SiN_x) layer was sputtered in the presence of oxygen (Ar: O₂ - 4: 1 and flow rate 8 sccm (standard cubic centimeter per minute)), to improve its quality. This SiO₂ provided electrical isolation and also separation (gap, **g**) between the lower and upper nanoring electrodes in the final configuration.
- e) After the deposition of the first insulation layer, all the edges of the glass substrates were wrapped with Teflon tape and only a small rectangular area (~5 mm × 1 mm) in the middle was left unprotected. A 7 nm thick Ti adhesion layer was then sputtered over the defined area by the Teflon tape.
- f) Subsequently, the second Au layer (50 nm thick) was sputtered over the Ti layer on the designated region by the Teflon tape.
- g) Followed by sputtering of 7 nm adhesion Ti layer over the gold film.
- h) After this step, half side of the substrates was wrapped with the Teflon tape before the sputtering of the final 150 nm thick SiO₂ passivation layer. In this case, the Teflon tape protected the metal film regions on the substrates' edge, and the middle part served later as the electrical contact pads to the first and second gold layers, respectively. The final SiO₂ layer was then sputtered in the presence of the oxygen (Ar: O₂ - 4: 1 and flow rate 8 sccm (standard cubic centimeter per minute)), to improve its isolation quality. This layer provided the electrical isolation to the second gold layer (upper nanoring electrodes) and also defined the upper ring electrodes recessed depth on the final device.
- i) Finally, the recessed nanoring-ring electrodes array (3.3 μm × 3.3 μm) with $r = 150$ nm and the interelectrode distance of 600 nm were fabricated using FIB on the Ti (7nm) / Au (50 nm) / Ti (7 nm) / SiO₂ (150 nm) / Ti (7 nm) / Au (50 nm) / Ti (7 nm) /SiO₂ (150 nm) stack in the middle of the substrate.
- j) An NMR tube (which was cut to less than 8 mm length) was fixed over the Ti/Au /Ti/SiO₂/Ti /Au/Ti /SiO₂ stack containing the recessed nanoring-rings array with a dielectric epoxy and served as the electrochemical cell.

Figure S-2. Optimization of the FIB fabrication parameters using Z-contrast imaging

We followed the same procedure for the fabrication of the 6×6 Au-NRRA as those we explained in our previous work². Briefly, the FIB cut were defined with the following parameters: dwell time in microseconds (i.e. the amount of time the beam stays at a particular pixel point as it raster across the pattern) and N (the number of raster passes). Only the numbers of N were increased from array to array and the dwell time was kept constant. Next, the Z-contrast imaging (also called backscattering imaging) was used to find out which FIB conditions were the proper ones for the fabrication of Au-NRRA. Z-contrast imaging gives the elemental information in contrast to the SEM image which provides only the topographical information. In Z-contrast imaging the secondary electrons are filtered out, and the image shows the presence of different elements.

In contrast to our previous work², in which we had to be very careful to find the proper parameters for the fabrication of the disc electrodes. (We had to stop cutting right after the appearance of the Au-disc). Here, the primary concern was to mill deep enough, all the way through all the four layers of insulator/metal/insulator/metal and to reach the glass substrate. (Here, reaching the glass substrate was a proper indication that we had cut deep enough, though all four layers). Z-contrast imaging allowed us to achieve this goal with confidence. Since the Z-contrast imaging shows the different materials used in the fabrication (SiN_x as the first (*l*) and second (*g*) insulator layers, Au as the first and second metal layers, and the glass substrate) in different colors.



Simulation Details

We have performed both 3D and 2D simulations on 6×6 Au-NRRA operating in either single or dual mode, respectively. Simulations were carried out using a commercial finite-element software package (COMSOL Multiphysics[®] ver. 5.2). The 2D simulations were run on our PC workstation with 32.0 GB RAM (Lenovo Thinkstation), and the 3D simulations were run on WestGrid and Compute Canada clusters. In all the simulation studies, the recess depth (the first insulator layer's thickness), l was kept constant, 150 nm. The height of both upper, h_c , and lower, h_g , ring electrodes, the nanoholes' radius, r , and the interelectrode gap (g) were changed to study the effect of these parameters on the array performance. The active area of the upper and lower nanorings was kept identical to each other in all the simulation studies. In the redox cycling studies, depicted in Fig. 1b of the main manuscript, the lower nanoring electrodes act as generator electrodes at which the potential was swept between 0.3 and -0.3 V, at a sweep rate of 0.05 to 1000 Vs^{-1} , while, the potential of the upper nanoring electrodes, acting as the collector electrodes, was held at a constant oxidizing potential, 0.3 V. For the case without redox cycling, single mode, the upper ring was assumed to be an insulator layer. Therefore, the cyclic voltammetry simulations were conducted on an array of nanoholes containing only the recessed lower ring electrodes, Figure S-4. The recess depth of the nanoring electrodes in single mode corresponds to the depth of the lower ring in dual mode, which is the summation of the thicknesses of the top insulating layer, upper ring height and the gap between the rings pair in the case of dual mode, Figure S-4, to accurately investigate the extent of redox cycling effect on the current response of the lower ring in single and dual modes (the current amplification factor). For the single mode, the simulations have been performed in 3D domains; detailed information on the simulation is given in our previous work². Briefly, Figure S-3a shows the 2D slice concentration profile of species O on the first row of a 6×6 recessed nanoring electrodes array. Figure S-3a illustrates that recessed nanorings array at single mode operation experiences a radial diffusion over the whole array due to the small size of the entire array when the diffusion zones among the adjacent nanoholes extremely overlap. As a result, the whole array behaves like a single microelectrode with the same size of the array with a steady state response. Considering the overall radial shape of the diffusion layer over the whole array the contribution of each nanohole electrode to the overall response of the array is different from each other, and it

depends a lot on where the nanohole is located in the array. Therefore, the 2D simulation based on the diffusion domain approximation³ cannot provide satisfactory results and a 3D simulation is required to be performed in order to study the voltammetric response of the micrometer-sized array accurately⁴. Detailed information on the 3D simulation in the COMSOL is given in our previous report².

In dual mode (redox cycling mode), the potential of the lower ring (generator) was scanned between 0.3 and -0.3 V, and the upper ring (collector) was held at a fixed oxidizing potential, 0.3 V, such that redox species generated at the lower electrode was reoxidized to starting material at the upper electrode. The cycling of the redox species between recessed ring-ring electrodes totally eliminated the overlap of the diffusional fields of adjacent nanoholes (containing ring-ring pair), Figure S-3b. Since the nanoholes (containing ring-ring generator-collector pair) electrodes are diffusionally independent, the response of only one ring-ring pair needs to be simulated, Figure S-5. Furthermore, the cylindrical symmetry of the electrodes allowed the simulation of half of the nanorings pair electrodes. Hence, the redox cycling simulations at the ring-ring generator-collector pair electrodes were carried out over two-dimensional domains, based on the diffusion domain approximation³.

The cyclic voltammetry was performed at the lower ring electrode (generator), and the simulation of a simple reversible redox reaction was considered at this electrode accordingly:



while the upper ring electrode (collector) was subjected to a fixed potential to oxidize the species B back to its starting form:



where A and B are both soluble species, which are $Fe(CN)_6^{3-}$ and $Fe(CN)_6^{4-}$ respectively in this current study, but only species A is supposed to be present in the solution with an initial bulk concentration of 20 mM.

The rate of electron transfer is given by the Butler-Volmer kinetics:

$$D_A \left. \frac{\partial c_A}{\partial r} \right|_{el} = (k_f c_A - k_b c_B) \Big|_{el} \quad (3)$$

Where $D_A \frac{\partial c_A}{\partial r} \Big|_{el}$ is the diffusional flux of species A to the electrode surface, and k_f and k_b , the forward and reverse reaction rate constants, respectively, and they are described as:

$$k_f = k^0 \exp\left(-\frac{\alpha F}{RT}(E - E^{\hat{0}})\right) \quad (4)$$

$$k_b = k^0 \exp\left(\frac{(1-\alpha)F}{RT}(E - E^{\hat{0}})\right) \quad (5)$$

k^0 is the heterogeneous rate constant for the redox couple, taken as 10^{-2} ms^{-1} , and $E^{\hat{0}}$ is the formal electrode potential, set at 0.25 V .⁴ E is the potential applied to the electrode. α is the effective transfer coefficient, assumed to be 0.5. The temperature, T , fixed at 298 K . R and F are the universal gas constant the Faraday's constant, respectively

The diffusion of the redox species is characterized by the following equation:

$$\frac{\partial c}{\partial t} = \nabla \cdot (D\nabla c) \quad (6)$$

where c is the concentration and D is the diffusion coefficient (assumed equal for both species), set as $6.5 \times 10^{-10} \text{ m}^2 \text{ s}^{-1}$.⁴ This equation assumes that the transport of O and R is solely controlled by diffusion, a valid approximation, considering an excess of supporting electrolyte is present so that migration is negligible. The bulk solution condition is assigned at the outer boundary of the model, at a distance $6\sqrt{t_{\text{tot}}D}$, from the electrode surface where t_{tot} is the total simulation time. Beyond this, the influence of the domain size on the simulation result is not significant.

Figure S-3. a) 2D slice concentration profile for a 6×6 recessed nanoring microarray, no redox cycling. (The 6×6 Au-NRRA configuration operating in single mode). b) Simulated concentration profile for a 6×6 Au-NRRA operating in redox cycling mode. The hole radius ($r = 150$ nm), ring height ($h = 50$ nm), scan rate ($v = 0.05$ Vs^{-1}), interelectrode distance (600 nm), were the same for both array. The recessed depth of ring electrodes in a) was 350 nm, which coincides with the recessed depth of lower ring in ring-ring geometry, Figure S-4. The recessed depth was ($l = 150$ nm), and ring gap was ($g = 150$ nm) in the ring-ring array geometry. The concentration profiles were obtained for the species O at the potential in which the steady-state current was established, on the forward scan

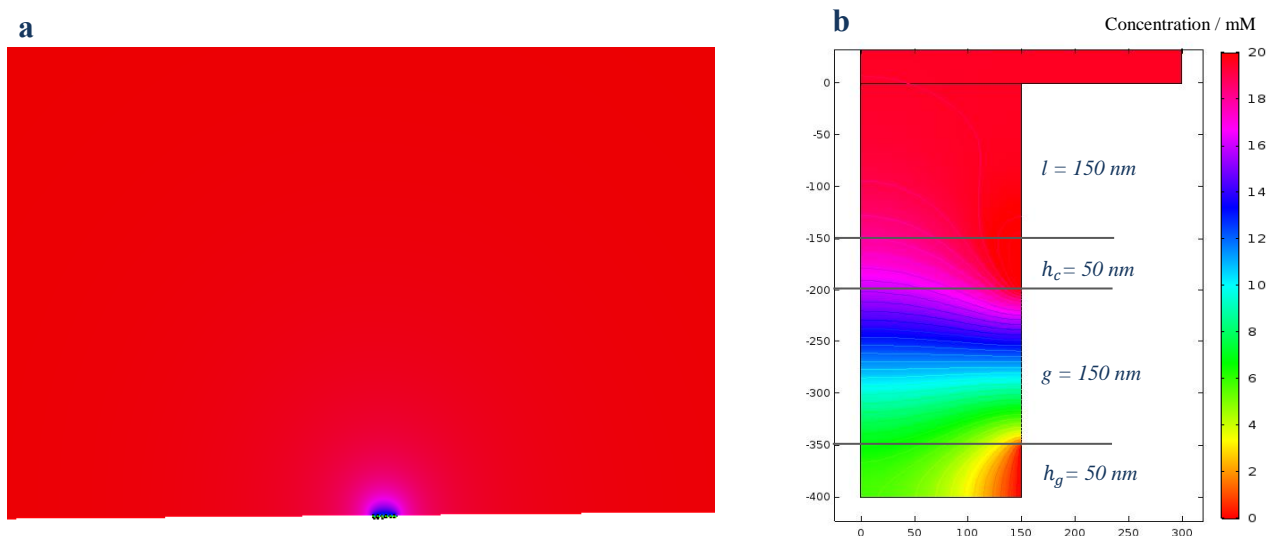


Figure S-4. Schematic representations of a) 6×6 recessed generator-collector nanoring-ring microarray b) 6×6 recessed nanorings microarray (recessed nanoring-ring microarray operating in single mode). Recessed depth, l , collector height, h_c , nanoring's pair gap, g , generator height, h_g , and ring height, h , are indicated in Figures. Magnitude of the recessed depth, l , in 6×6 recessed nanorings microarray (recessed nanoring-ring microarray operating in single mode) corresponds to the summations of the values of l and h_c and g in Figure S-4a.

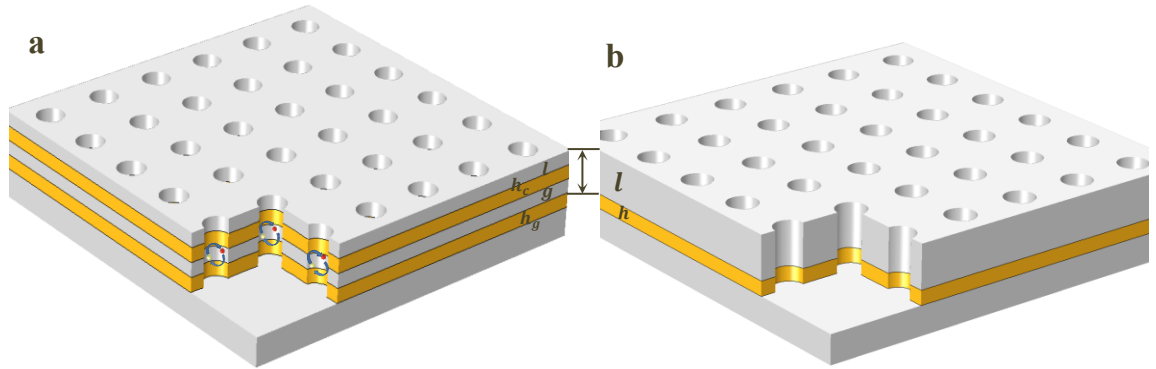


Figure S-5. a) Schematic representation of the unit cell for a 6×6 Au-NRRA; b) individual unit cell in Cartesian coordinates; c) equivalent diffusion domain approximation in cylindrical coordinates; d) sketch of the 2D simulation space used for the simulation of recessed nanoring-ring; and e) close-up 2D model of the simulation space and f) its meshing. ($2\times R$ = interelectrode distance)

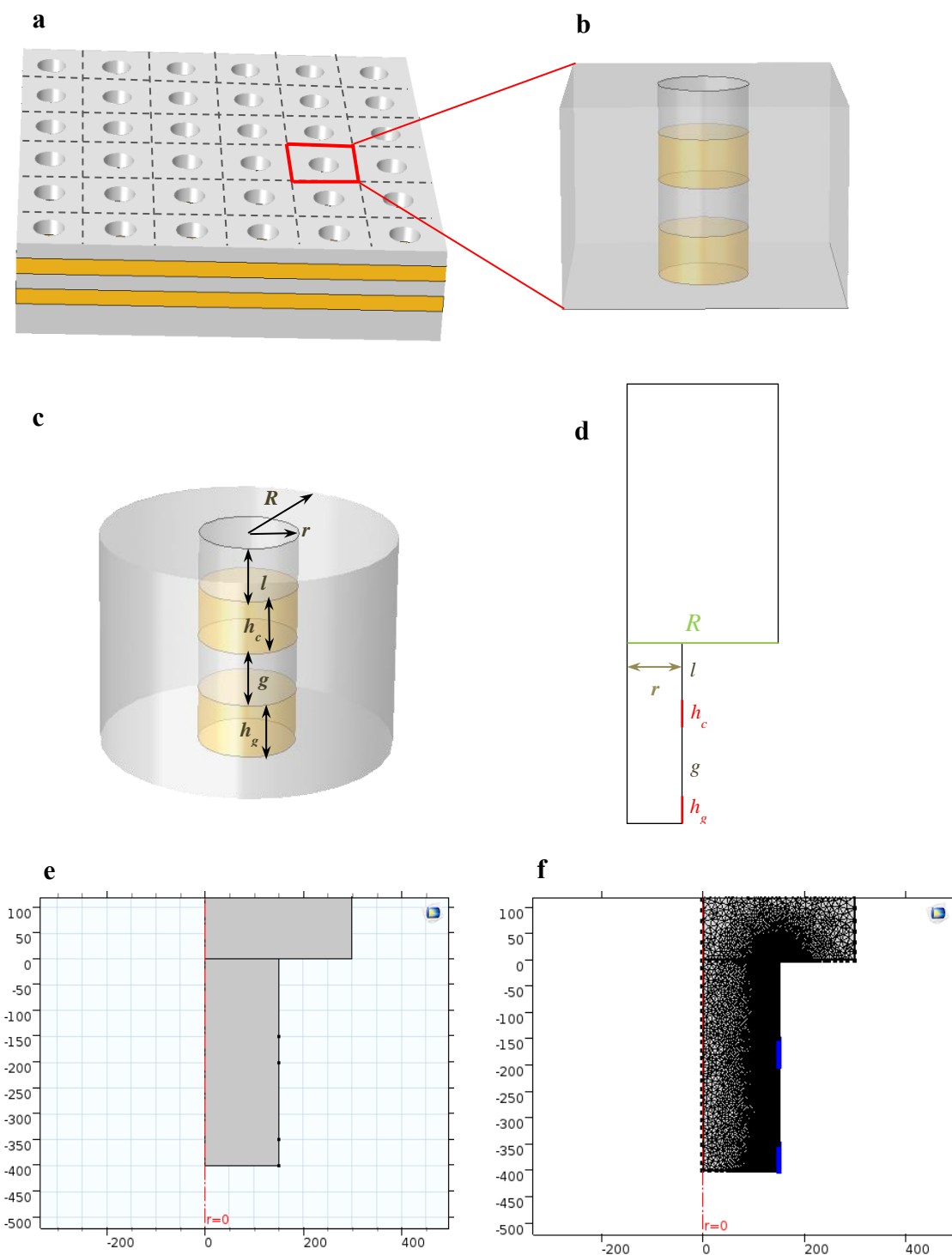


Figure S-6. Comparison of simulation results for cyclic voltammograms represented base on the limiting current and current density for the 6×6 Au-NRRAs with different ring's heights, 25 nm, 50 nm, 75 nm, and 100 nm, operating in redox cycling mode. The height of lower ring (generator) and upper ring (collector) was kept the same in all of the simulations. The scan rate ($\nu = 0.1 \text{ Vs}^{-1}$) and hole radius A) and a) $r = 100 \text{ nm}$; B) and b) $r = 150 \text{ nm}$; C) and c) $r = 200 \text{ nm}$ were kept constant in S-6A, a; S-6B, b; and S-6C, c; respectively. The rest of parameters used are given in the main text.

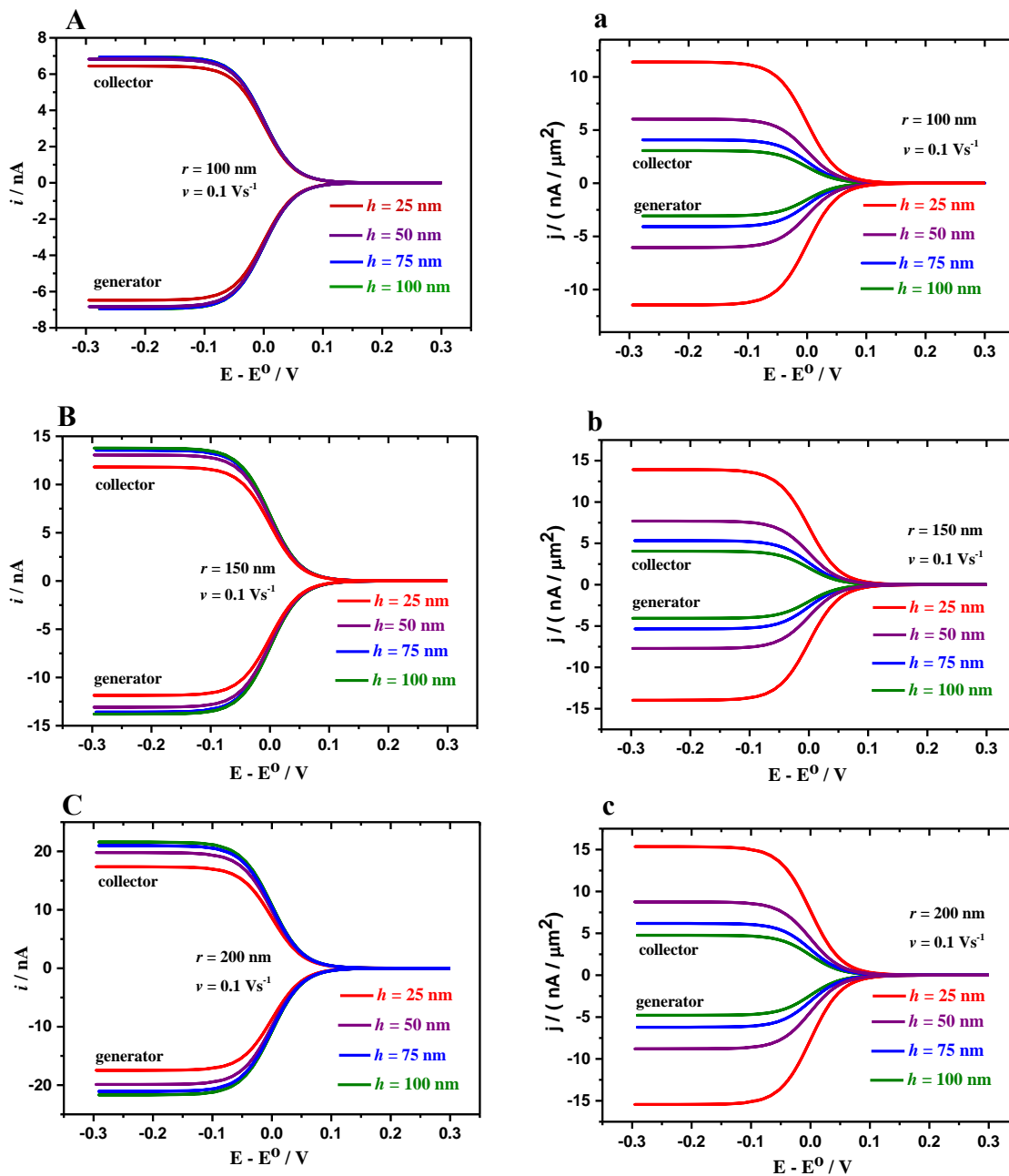


Table S-1. Influence of the varying ring height on the 6×6 Au-NRRA performance, Table S-1a) $r = 100$, Table S-1b) $r = 150$ nm, and Table S-1c) $r = 200$ nm. The simulation parameters were the same as those in Figure S-6.

a

h / nm $r = 100$	i_{GE} / nA	$i_{GE_{cycl}} / \text{nA}$	$j_{GE_{cycl}} / \text{nA}/\mu\text{m}^2$	i_{CE} / nA	$j_{CE} / \text{nA}/\mu\text{m}^2$	$\eta / \%$	A_f
25	-2.069	-6.47	-11.44	6.44	11.40	99.54	3.1
50	-2.068	-6.83	-6.04	6.82	6.03	99.85	3.3
75	-	-6.94	-4.09	6.93	4.08	99.85	-
100	-1.953	-6.95	-3.07	6.95	3.07	100	3.6

Limiting current: increasing the ring height from $h = 25$ nm to $h = 50$ nm resulted in an increase of 5.6 %, from $h = 50$ nm to $h = 75$ nm resulted in an increase of about 1.61 %, and from $h = 75$ nm to $h = 100$ nm led to an increase of about 0.14 %, in the limiting current value.

Current density: increasing the ring height from $h = 25$ nm to $h = 50$ nm resulted in a decrease of about 47.2 %, from $h = 50$ nm to $h = 75$ nm resulted in a decrease of about 32.3 %, and from $h = 75$ nm to $h = 100$ nm resulted in a decrease of about 24.9 %, in the current density value.

b

h/nm $r = 150$	i_{GE} / nA	$i_{GE_{cycl}} / \text{nA}$	$j_{GE_{cycl}} / \text{nA}/\mu\text{m}^2$	i_{CE} / nA	$j_{CE} / \text{nA}/\mu\text{m}^2$	$\eta/\%$	A_f
25	-3.649	-11.85	-13.97	11.81	13.93	99.67	3.2
50	-3.743	-13.08	-7.71	13.06	7.69	99.85	3.5
75	-3.708	-13.59	-5.34	13.56	5.32	99.78	3.7
100	-3.637	-13.79	-4.06	13.77	4.05	99.85	3.8

Limiting current: increasing the ring height from $h = 25$ nm to $h = 50$ nm resulted in an increase of 10.4 %, from $h = 50$ nm to $h = 75$ nm resulted in an increase of about 3.9 %, and from $h = 75$ nm to $h = 100$ nm led to an increase of about 1.5 %, in the limiting current value.

Current density: increasing the ring height from $h = 25$ nm to $h = 50$ nm resulted in a decrease of about 44.8 %, from $h = 50$ nm to $h = 75$ nm resulted in a reduction of about 30.7 %, and from $h = 75$ nm to $h = 100$ nm led to a decrease of about 26.7 %, in the current density value.

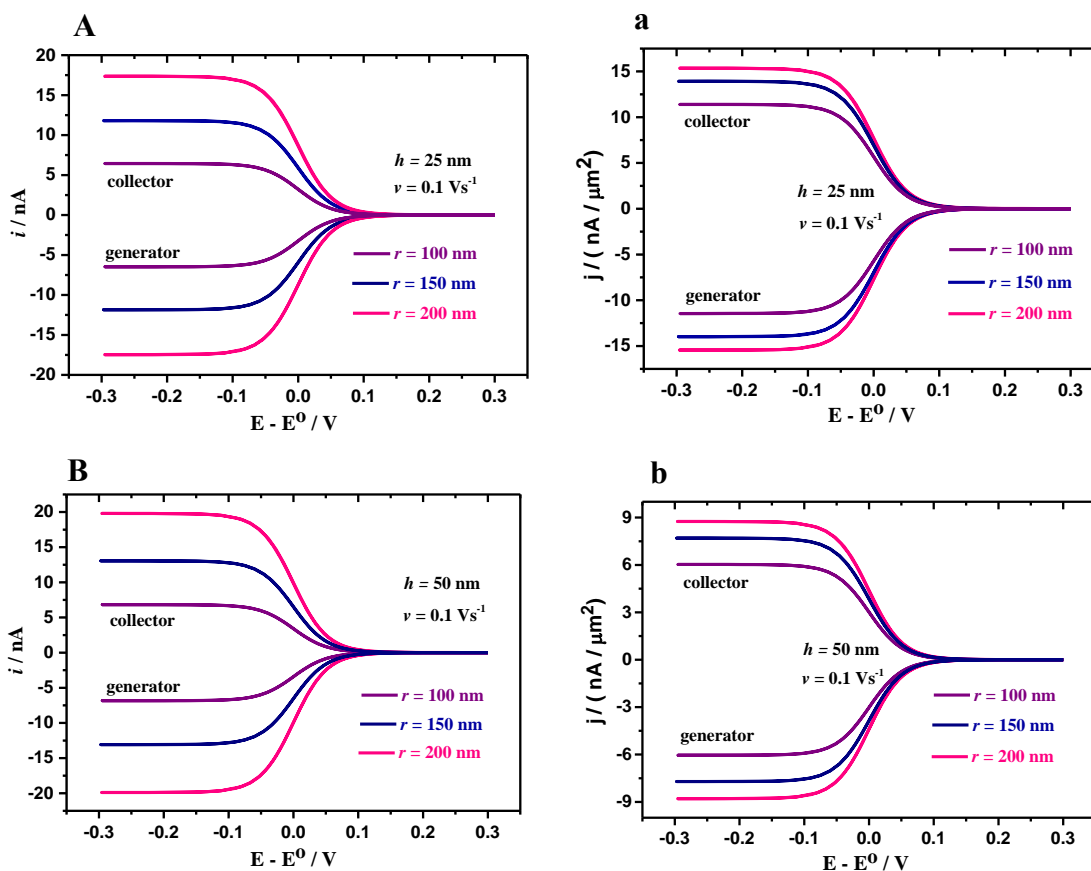
c

h / nm $r = 200$	i_{GE} / nA	$i_{GE_{cycl}} / \text{nA}$	$j_{GE_{cycl}} / \text{nA}/\mu\text{m}^2$	i_{CE} / nA	$j_{CE} / \text{nA}/\mu\text{m}^2$	$\eta / \%$	A_f
25	-5.288	-17.46	-15.44	17.36	15.35	99.42	3.3
50	-5.523	-19.89	-8.79	19.82	8.75	99.64	3.6
75	-5.536	-21.05	-6.20	20.99	6.19	99.71	3.8
100	-5.481	-21.67	-4.79	21.61	4.77	99.72	3.9

Limiting current: increasing the ring height from $h = 25$ nm to $h = 50$ nm resulted in an increase of 13.9 %, from $h = 50$ nm to $h = 75$ nm resulted in an increase of about 5.8 %, and from $h = 75$ nm to $h = 100$ nm led to an increase of about 2.9 %, in the limiting current value.

Current density: increasing the ring height from $h = 25$ nm to $h = 50$ nm resulted in a decrease of about 43 %, from $h = 50$ nm to $h = 75$ nm resulted in a decrease of about 29.5 %, and from $h = 75$ nm to $h = 100$ nm resulted in a decrease of about 22.9 %, in the current density value.

Figure S-7. Comparison of simulation results for cyclic voltammograms represented base on the limiting current and current density for the 6×6 Au-NRRA with different hole radiuses, 100 nm, 150 nm, and 200 nm, operating in redox cycling mode. The scan rate ($\nu = 0.1 \text{ Vs}^{-1}$) and ring heights A) and a) $h = 25 \text{ nm}$; B) and b) $h = 50 \text{ nm}$; C) and c) $h = 75 \text{ nm}$; D and d) $h = 100 \text{ nm}$ were kept constant in S-7A, a; S-7B, b; S-7C, c; and S-7D, d; respectively. The height of lower ring, generator, and upper ring, collector, were kept the same in all of the simulations. The rest of the simulation parameters were the same as those in Figure S-6.



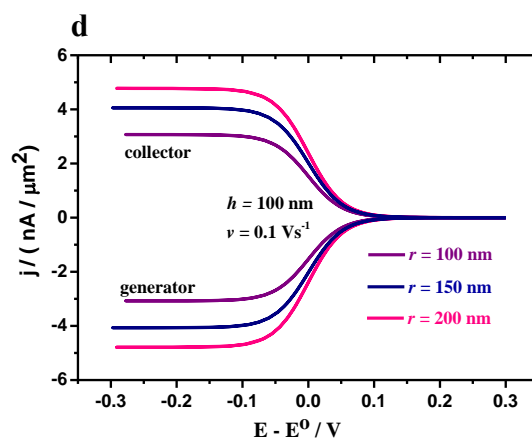
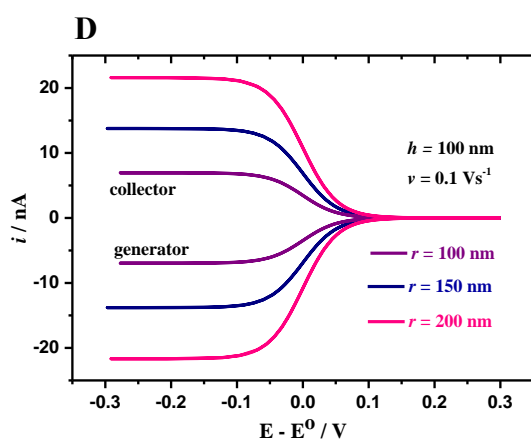
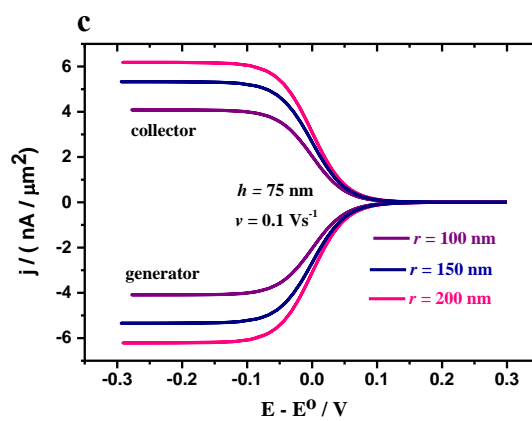
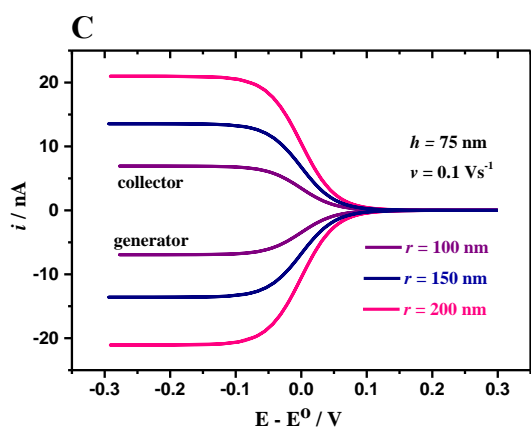
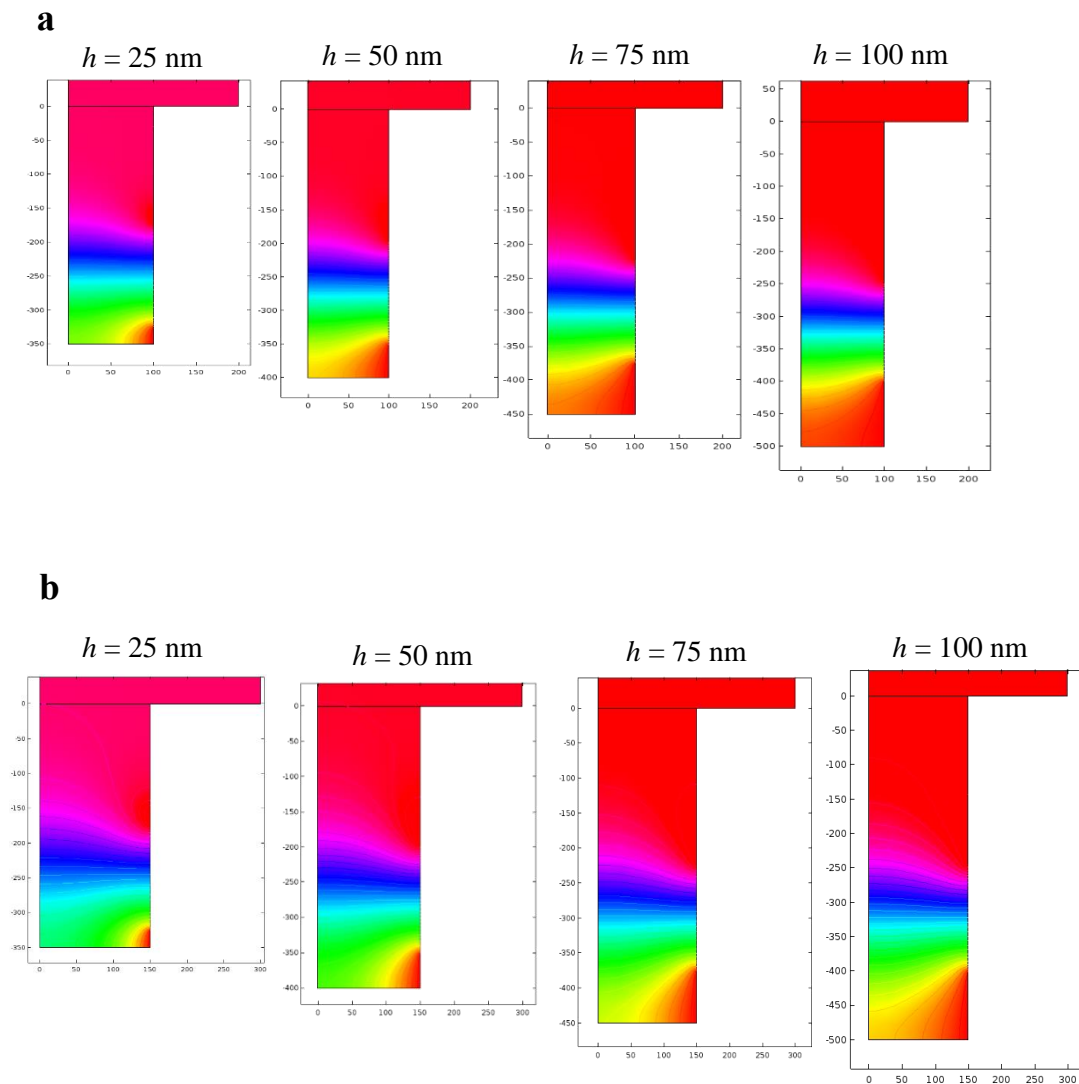


Figure S-8. Surface concentration profiles for species O within the hole next to the electrode surface for the Au-NRRA with different heights (25 nm, 50 nm, 75 nm, 100 nm). The concentration profile images were taken at the steady state potentials. The hole radius a) $r = 100$ nm, b) $r = 150$ nm c) $r = 200$ nm, and the scan rate ($v = 0.1 \text{ Vs}^{-1}$) were the same for each set a, b, and c, respectively.



c

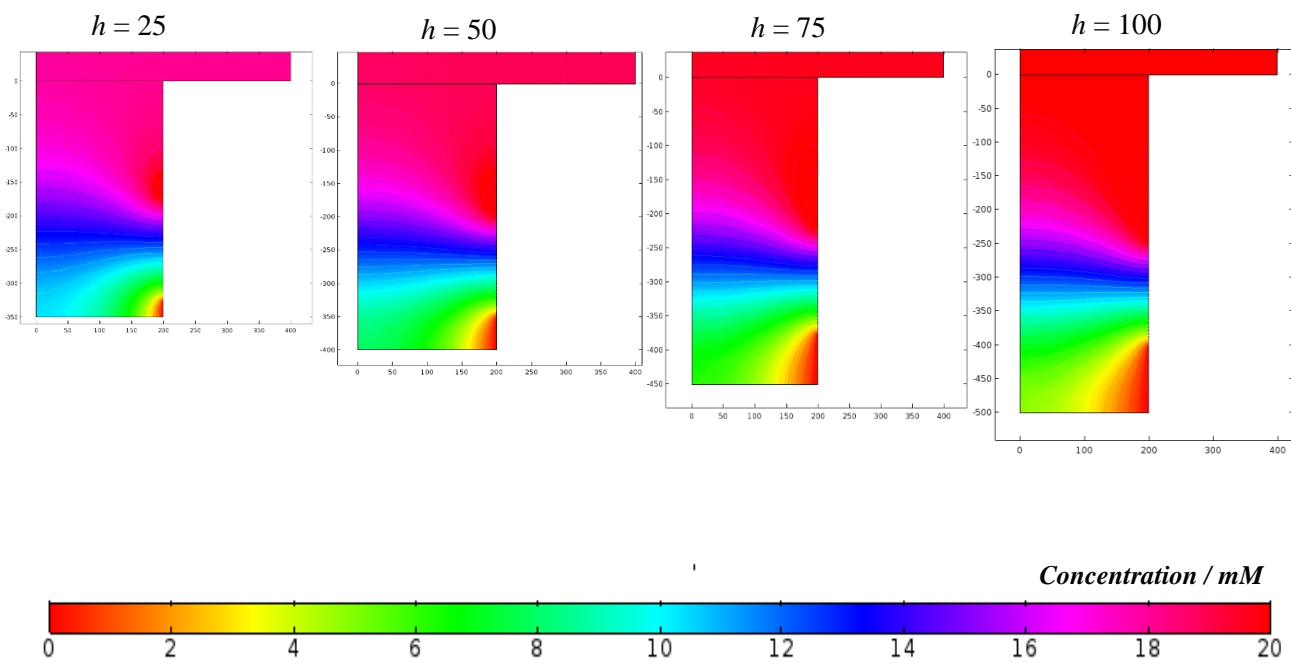
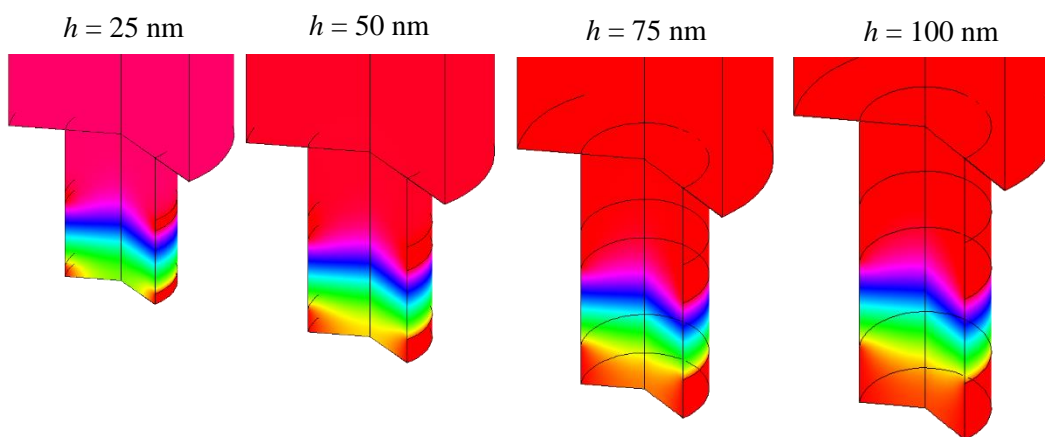
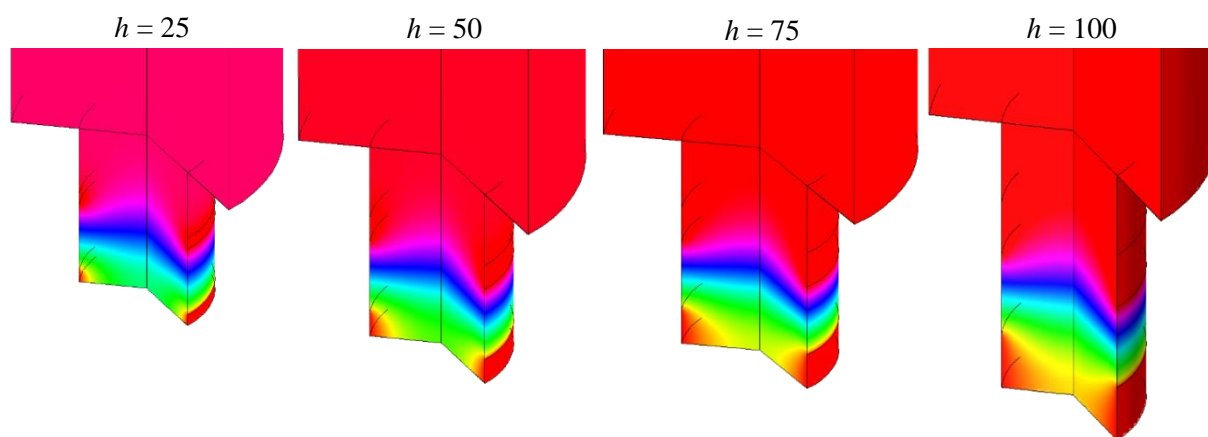


Figure S-9. Volume concentration profiles (revolution 2D) for species O within the hole next to the electrode surface for the Au-NRRA with different heights (25 nm, 50 nm, 75 nm, 100 nm). The concentration profile images were taken at the steady state potentials. The hole radius a) $r = 100$ nm, b) $r = 150$ nm c) $r = 200$ nm, and the scan rate ($v = 0.1 \text{ Vs}^{-1}$) were the same for each set a, b, and c, respectively.

a



b



c

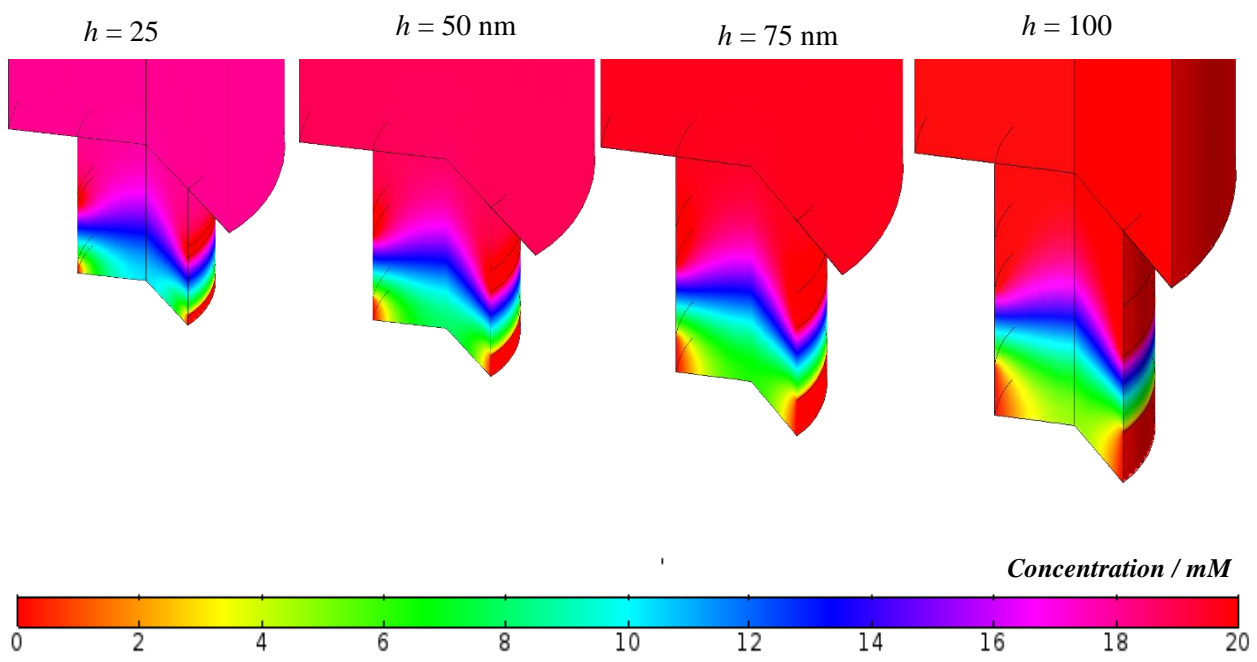


Figure S-10. Simulated cyclic voltammograms under various scan rates for a 6×6 Au-NRRA operating in A and B) redox cycling mode, and a and b) single mode. The ring height ($h = 50$ nm), and the interelectrode distance were set ($4r$) in all the simulations. The recessed depth ($l = 150$ nm) and ring gap ($g = 150$ nm) were the same for all the simulations in A) and B). The recessed depth was ($l = 350$ nm) in a) and b), which coincide with the recessed depth of lower ring in ring-ring geometry, Figure S-4. The hole radius was $r = 100$ nm in A and a) and it was $r = 200$ nm in B and b). In single mode simulations, the potential of lower rings were swept between 0.3 and -0.3 V at different scan rates ranging from 0.05 Vs^{-1} up to 1000 Vs^{-1} and the upper ring electrodes were considered as insulator layers. In dual mode, the lower ring (generator) potential was swept in the same way as in the single mode, at a sweep rate of 0.05 - 1000 Vs^{-1} while the upper ring potential (collector) was kept constant at 0.3 V . The rest of simulation conditions are given in the main text.

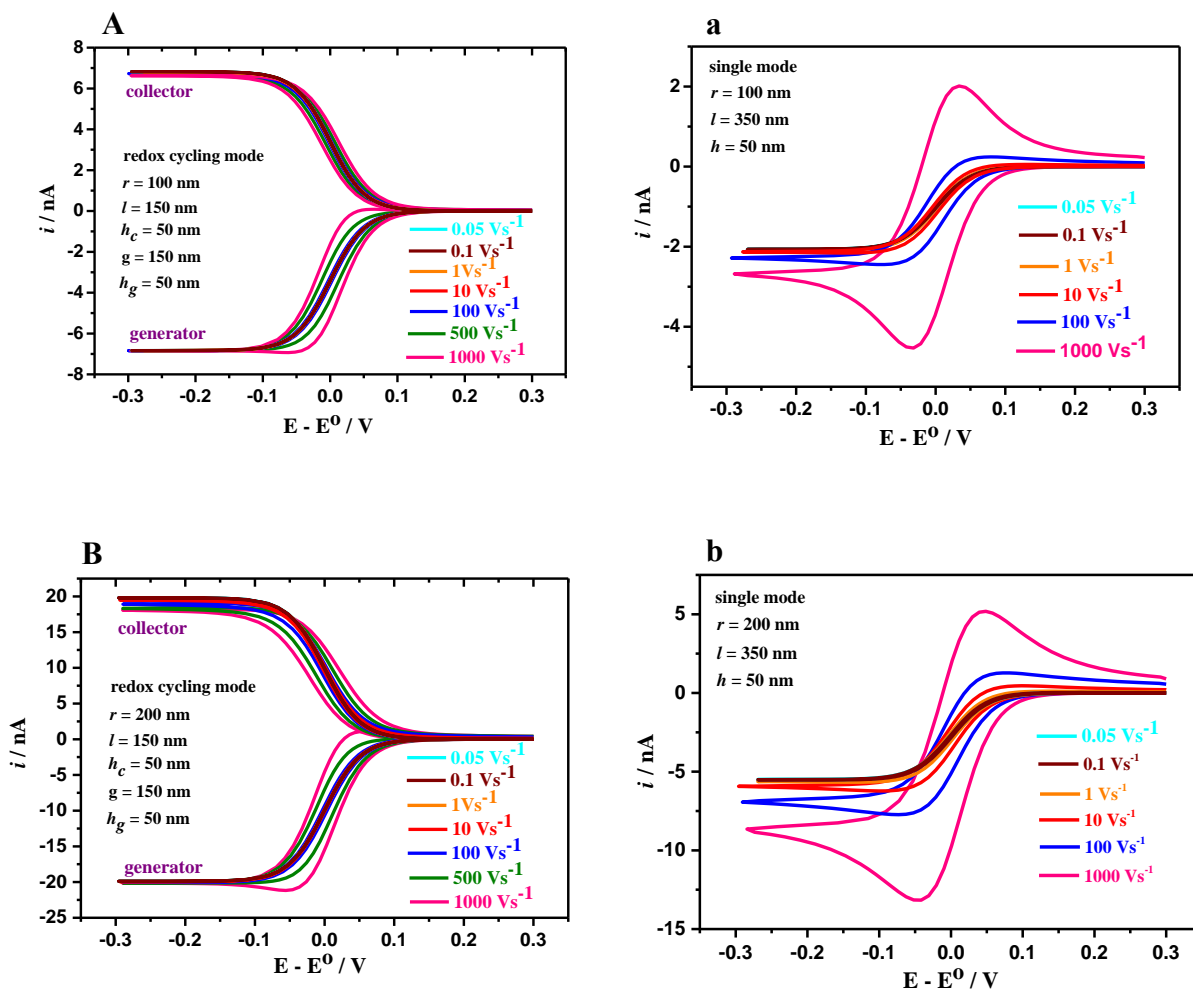


Table S-2. Influence of the scan rate on the 6×6 Au-NRRA performance, a) $r = 100$ and b) $r = 200$ nm. The simulation conditions are the same as Figure S-10.

a

Scan rate /Vs ⁻¹	i_{GE} /nA	$i_{GE_{cycl}}$ /nA	i_{CE} /nA	η /%	A_f
0.05	-2.065	-6.834	6.822	99.82	3.31
0.1	-2.067	-6.834	6.821	99.81	3.31
1	-2.087	-6.837	6.811	99.62	3.28
10	-2.159	-6.838	6.792	99.33	3.17
100	-2.447	-6.841	6.736	98.46	2.79
1000	-4.533	-6.933	6.635	95.70	1.53

b

Scan rate /Vs ⁻¹	i_{GE} /nA	$i_{GE_{cycl}}$ /nA	i_{CE} /nA	η /%	A_f
0.05	-5.504	-19.890	19.809	99.59	3.6
0.1	-5.522	-19.892	19.799	99.53	3.6
1	-5.669	-19.906	19.734	99.14	3.5
10	-6.227	-19.947	19.531	97.91	3.2
100	-7.732	-20.052	19.018	94.84	2.6
1000	-13.16	-21.119	18.196	86.16	1.6

Figure S-11. Comparison of simulated cyclic voltammograms for the 6×6 Au-NRRAs (operating in redox cycling mode) with different inter-electrode gaps, 25 nm, 50 nm, 100 nm, 150 nm, 250 nm, 350 nm, at different scan rates: a) $\nu = 0.1 \text{ V s}^{-1}$ b) $\nu = 100 \text{ V s}^{-1}$ and c) $\nu = 1000 \text{ V s}^{-1}$. The hole radius ($r = 150 \text{ nm}$), recessed depth ($l = 150 \text{ nm}$), ring height ($h_c = h_g = 50 \text{ nm}$), and the interelectrode distance ($4r$) were the same in all the simulations.

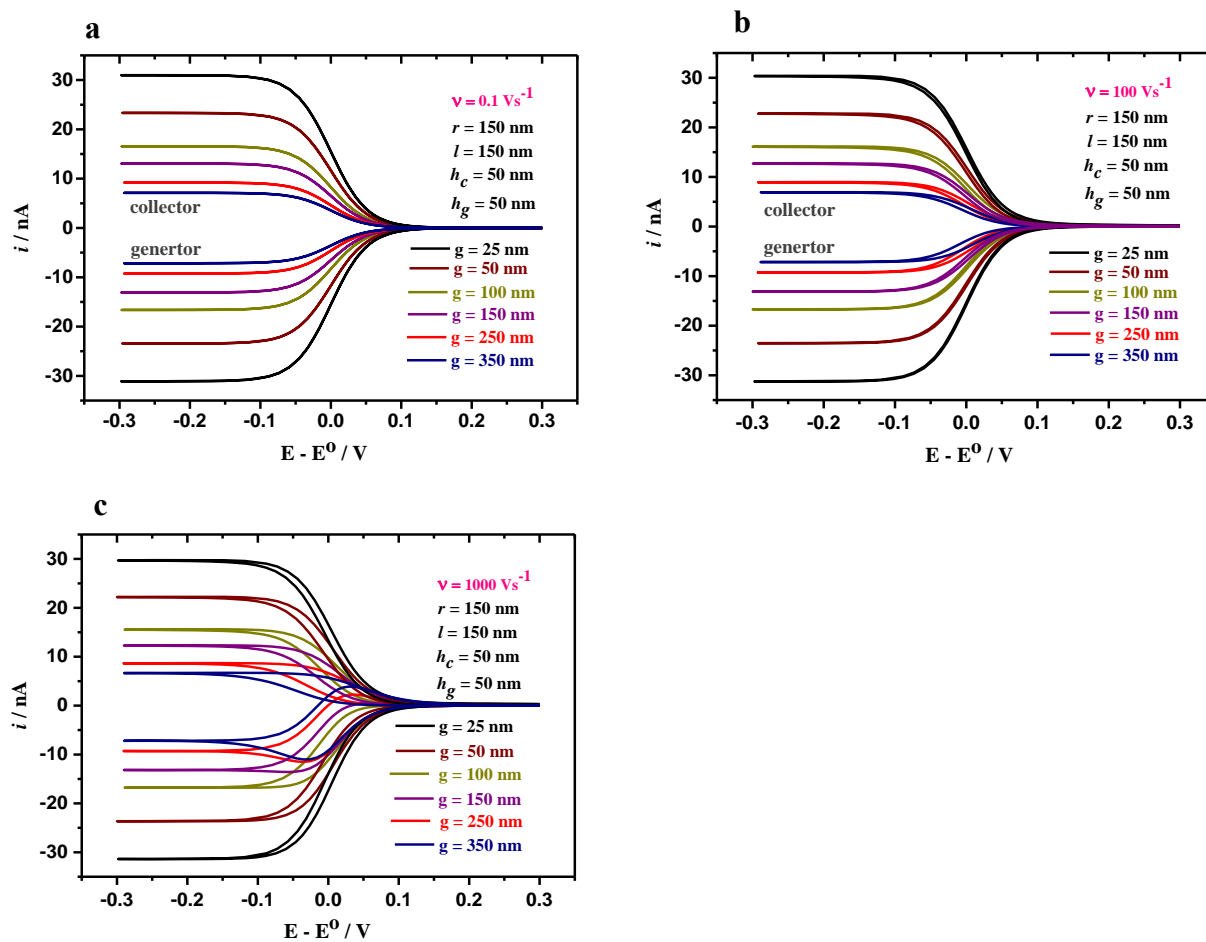


Figure S-12. Simulated cyclic voltammograms under various scan rates for a 6×6 Au-NRRA operating in redox cycling mode. The hole radius ($r = 150$ nm), recessed depth ($l = 150$ nm), ring height ($h_c = h_g = 50$ nm), and the inter-electrode distance ($4r$) were the same in all the simulations. The interelectrode gap was a) 25 nm, b) 50 nm, c) 100 nm, d) 150 nm, e) 250 nm, f) 350 nm.

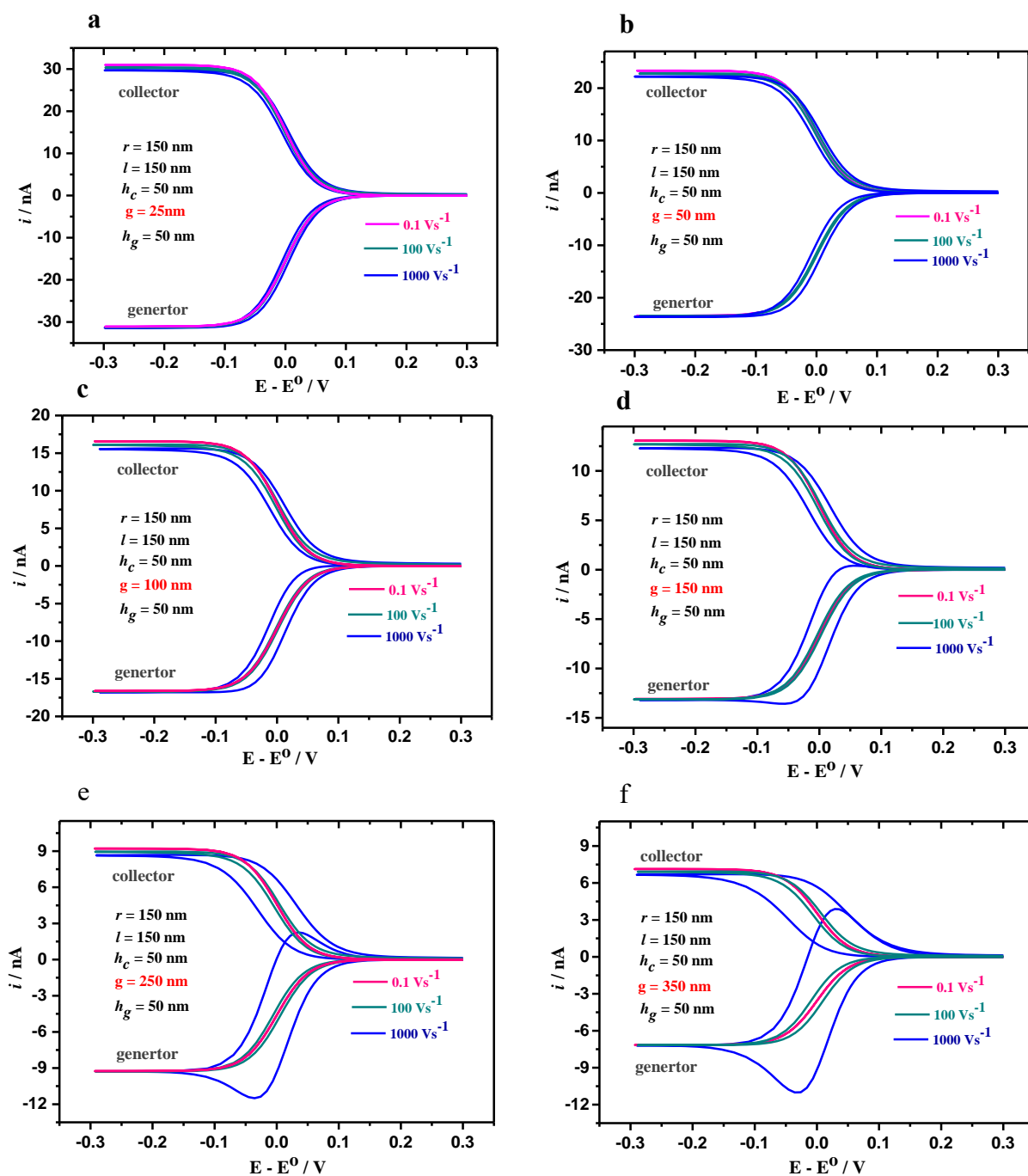


Figure S-13. Dependence of the limiting current on the interelectrode gap (the gap between generator and collector electrodes). Scan rate $\nu = 0.1 \text{ Vs}^{-1}$. The simulation parameters' are the same as Figure S-11 and S-12. (Note the electrodes' surface areas are the same in all these simulated arrays of different inter-electrode gap). As can be seen from this graph, the current response of the 6×6 Au-NRRA configuration operating in dual mode increases as the inter-electrode gap decreases, as it was expected.

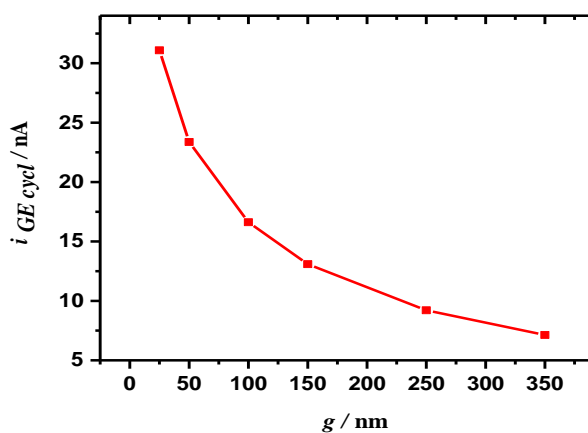


Table S-3. Influence of the interelectrode gap on the 6×6 Au-NRRA performance. The simulation conditions are the same as Figure S-11 and S-12.

Interelectrode gap/nm	Scan rate Vs^{-1}	$i_{GE_{cycl}}/nA$	i_{CE}/nA	$\eta/\%$
25	0.1	-31.09	30.99	99.67
25	100	-31.25	30.39	97.25
25	1000	-31.39	29.75	94.78
50	0.1	-23.44	23.37	99.70
50	100	-23.53	22.89	97.28
50	1000	-23.65	22.24	94.04
100	0.1	-16.62	16.56	99.64
100	100	-16.68	16.19	97.06
100	1000	-16.79	15.62	93.03
150	0.1	-13.08	13.06	99.85
150	100	-13.11	12.73	97.10
150	1000	-13.57	12.33	90.86
250	0.1	-9.25	9.21	99.56
250	100	-9.27	8.97	96.76
250	1000	-11.50	8.69	75.56
350	0.1	-7.15	7.13	99.72
350	100	-7.17	6.93	96.65
350	1000	-11.01	6.70	60.85

Figure S-14. Surface concentration profiles for species O within the hole next to the electrode surface for the Au-NRRA with different interelectrode gaps (25 nm, 50 nm, 100 nm, 150 nm, 250 nm, 350 nm). The concentration profile images were taken at the steady state potentials. The hole radius ($r = 150$ nm), recessed depth ($l = 150$ nm), ring height ($h_c = h_g = 50$ nm), the scan rate ($v = 0.1$ Vs⁻¹), and the interelectrode distance ($4r$) were the same in all the simulations.

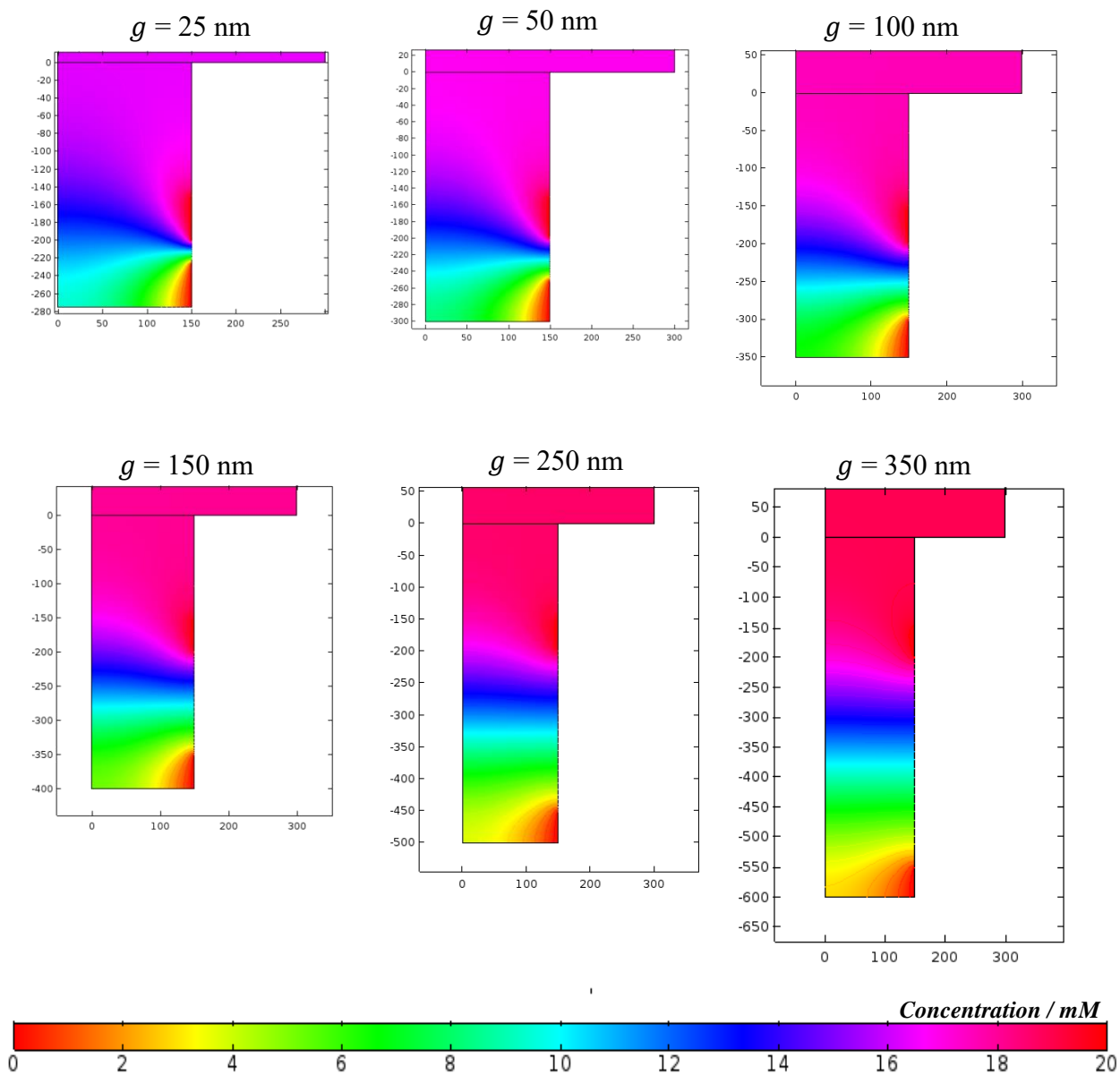
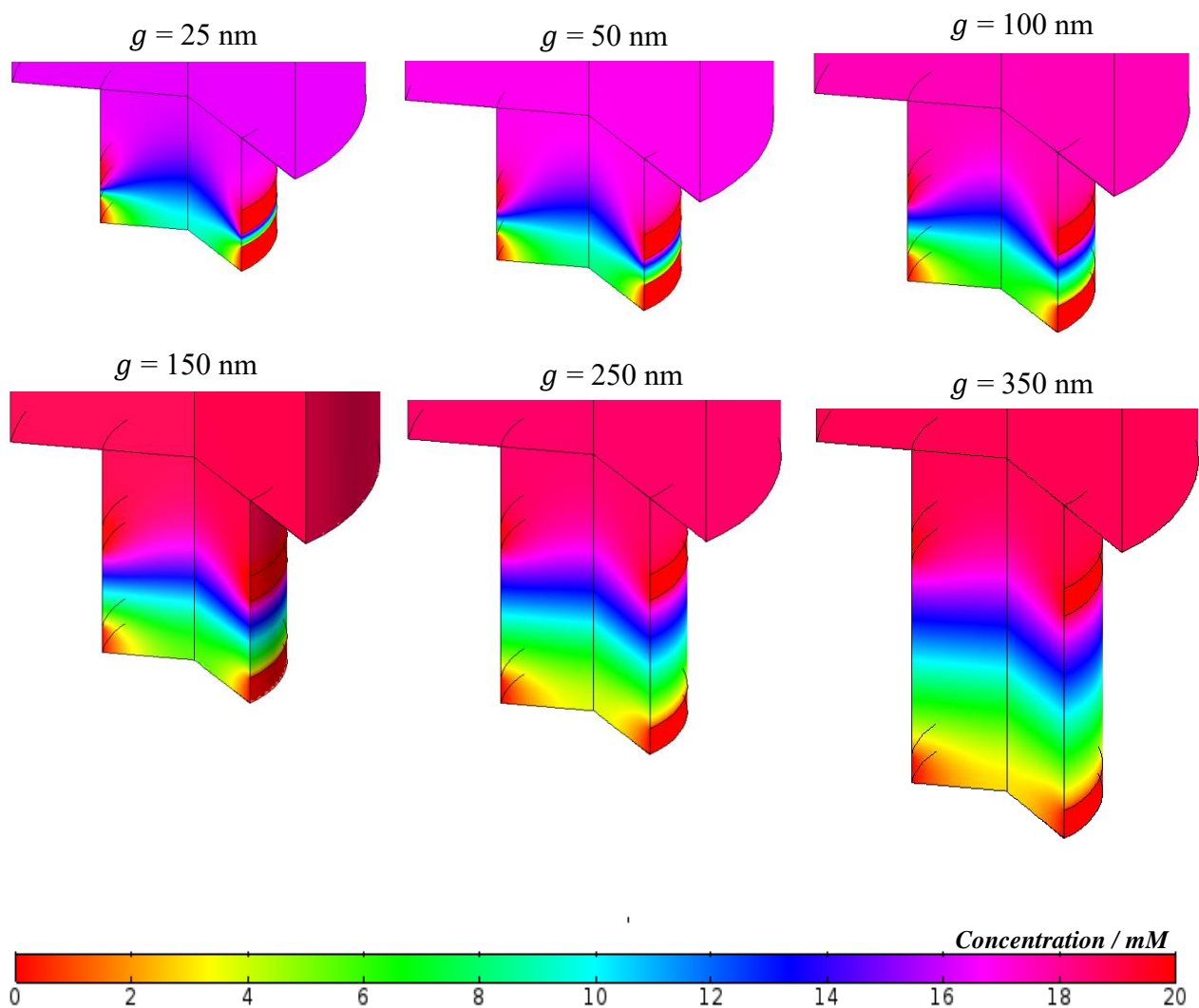


Figure S-15. Volume concentration profiles (revolution 2D) for species O within the hole next to the electrode surface for the Au-NRRA with different interelectrode gaps (25 nm, 50 nm, 100 nm, 150 nm, 250 nm, 350 nm). The concentration profile images were taken at the steady state potentials. The hole radius ($r = 150$ nm), recessed depth ($l = 150$ nm), ring height ($h_c = h_g = 50$ nm), the scan rate ($v = 0.1 \text{ Vs}^{-1}$), and the interelectrode distance ($4r$) were the same in all the simulations.



Notes on the amplification factor

The amplification factor (A_f), as defined in eq. 2 in the main manuscript, is one of the parameters widely used to evaluate the performance of a redox cycling system. However, this factor is not often a proper parameter for a direct comparison between the performances of different redox cycling structures. The inefficiency of this factor for directly comparing the performance of different configurations arises from its definition. A_f basically compares the behavior of a specific system under investigation (a set of electrodes or arrays of electrodes) operating in redox cycling mode to the same type of system operating in single mode. Since nanoelectrodes operate very efficiently in single mode, they might yield low A_f , even when the redox cycling significantly improves the performance. In another example, Wolfrum et al.⁵ have previously pointed out that this simple factor cannot be used to evaluate the performance of a small confined redox cycling system that generates a finite limiting current while operating in dual mode. Because in single mode due to the confined environment, the system can be completely depleted from the electroactive molecule of interest after all the molecules being oxidized or reduced and the current will approach zero. Since eq. 2 compares the behavior of a particular system operating in dual mode with itself when it is running under the single mode, the denominator here goes to zero and the amplification factor would tend to infinity.

In addition to being very dependable on the configuration of the system, A_f is also very dependent on the whole size of the array.

It is well known that the shape of the diffusion layer has a huge influence on the performance of an electrode. 3D diffusion enhances the mass transport at a small electrode (when the overall electrode size is smaller than the diffusion layer). The mass transport keeps improving as the electrode becomes smaller. In the case of a very small array of electrodes that can operate in redox cycling mode, like the ones studied in this manuscript, the current increases significantly in redox cycling mode. However, the current amplification will be calculated using the single mode operation from a small array that also benefits from enhanced mass transport, due to 3D diffusion layer.

We have investigated very small arrays of recessed nanoring-ring electrodes (6×6). The work was limited to small arrays to allow rigorous comparison to calculated results (large arrays would

be computationally expensive and very time-consuming). As we have shown, there is no significant diffusion layers overlap among the adjacent nanoholes on the array in redox cycling mode. The presence of the top ring confines the diffusion layer within each nanohole. Then using a larger array will improve the response of this device greatly, because the current response of each nanohole (containing the nanoring-ring electrodes) will simply add up.

On the other hand, as the whole size of the array increases the mechanism of mass transport at the array operating in single mode changes from spherical to the mixed spherical and linear diffusion and finally to the linear diffusion. As a result, as the array becomes larger, the A_f value for this device (Au-NRRA) will increase. This demonstrates that the amplification factor is very dependent on the properties of the array.

Next, using a very simple example, we will further illustrate the dependency of the A_f value on the whole size of the array. In Table S-4 we have estimated the A_f for arrays of four different sizes.

We have estimated the current of the array opening in single mode using eq. 7⁴. (The analytical solution for the recessed disc electrode).

$$I = \frac{4nFcDr_o}{\left(\frac{4L}{\pi r_o} + 1\right)} \quad (7)$$

Where n is the number of the transfer electrons, r_o is the electrode radius and L is the recess depth value. (Here, we considered the whole square array operating in single mode as a single disc electrode of identical surface area and estimated its current using eq. 7⁴). Table S-4 clearly shows that the estimated A_f values increase with the number of elements (size) of the array.

Another interesting aspect to be pointed out is the relationship between the amplification factor (A_f) and the number of redox cycles (N_{RC}), defined below:

$$N_{RC} = \frac{1}{1-\eta^2} \quad (8)$$

Where the collection efficiency of the collector electrode (CE) was considered the same as the collection efficiency at the generator electrode (GE), i.e., $\eta_{CE} = \eta_{GE} = \eta$

Niwa et al⁶ have shown that the value of N_{RC} approaches A_f for large values of average diffusion lengths (a few μm). In our case, the average diffusion length is very small. Therefore, the values of A_f and N_{RC} obtained experimentally from Figure 2 in the main manuscript are very different.

Table S-4. Demonstration of dependency of the amplification factor on numbers of the electrode available in redox cycling (the array size). The hole radius ($r = 150 \text{ nm}$) and the inter-electrode distance ($4r$).

Array size (μm)	Array size (# of electrodes)	Total # of electrodes	$i_{GE_{cycl}} / \text{nA}$ (Simulated results)	i_{GE} / nA (Simulated value)	Estimated i_{GE} / nA from eq. 7	A_f (Simulated value)	A_f (Estimated value)
$3.3 \mu\text{m} \times 3.3 \mu\text{m}$	6×6	36	13.08	3.74	6.52	3.5	2.01
$25.5 \mu\text{m} \times 25.5 \mu\text{m}$	43×43	1849	671.92	N/A	61.81	N/A	10.87
$50.1 \mu\text{m} \times 50.1 \mu\text{m}$	84×84	7056	2564.15	N/A	123.48	N/A	20.76
$100.5 \mu\text{m} \times 100.5 \mu\text{m}$	168×168	28224	10256.60	N/A	249.9	N/A	41.04

References

- (1) Han, D.; Zaino, L. P.; Fu, K. Y.; Bohn, P. W. *J. Phys. Chem. C* **2016**, 120, 20634-20641.
- (2) Atighilorestani, M.; Brolo, A. G. *Anal. Chem.* **2017**, 89, 6130-6136.
- (3) Davies, T. J.; Compton, R. G. *J. Electroanal. Chem.* **2005**, 585, 63-82.
- (4) Godino, N.; Borrise, X.; Munoz, F. X.; del Campo, F. J.; Compton, R. G. *J. Phys. Chem. C* **2009**, 113, 11119-11125.
- (5) Katelhon, E.; Wolfrum, B. *Rev. Anal. Chem* **2012**, 31, 7-14.
- (6) Niwa, O.; Morita, M.; Tabei, H. *Anal. Chem.* **1990**, 62, 447-452.